An Eccentric Massive Jupiter Orbiting a Subgiant on a 9.5-day Period Discovered in the *Transiting Exoplanet Survey Satellite* Full Frame Images

Joseph E. Rodriguez[1], Samuel N. Quinn[1], Chelsea X. Huang[2,29], Andrew Vanderburg[3,30], Kaloyan Penev[4], Rafael Brahm[5,6,7], Andrés Jordán[6,7], Mma Ikwut-Ukwa[1], Shelly Tsirulik[1], David W. Latham[1], Keivan G. Stassun[8,9], Avi Shporer[2], Carl Ziegler[10], Elisabeth Matthews[2], Jason D. Eastman[1], B. Scott Gaudi[11], Karen A. Collins[1], Natalia Guerrero[2], Howard M. Relles[1], Thomas Barclay[12,13], Natalie M. Batalha[14], Perry Berlind[1], Allyson Bieryla[1], L. G. Bouma[15], Patricia T. Boyd[12], Jennifer Burt[2,29], Michael L. Calkins[1], Jessie Christiansen[16], David R. Ciardi[16], Knicole D. Colón[12], Dennis M. Conti[17], Ian J. M. Crossfield[2], Tansu Daylan[2,31], Jason Dittmann[2,32], Diana Dragomir[2,33], Scott Dynes[2], Néstor Espinoza[18,34,35], Gilbert A. Esquerdo[1], Zahra Essack[19], Aylin Garcia Soto[19], Ana Glidden[2,19], Maximilian N. Günther[2,29], Thomas Henning[18], Jon M. Jenkins[20], John F. Kielkopf[21], Akshata Krishnamurthy[22], Nicholas M. Law[23], Alan M. Levine[2], Pablo Lewin[24], Andrew W. Mann[23], Edward H. Morgan[2], Robert L. Morris[20,25], Ryan J. Oelkers[8], Martin Paegert[1], Joshua Pepper[26], Elisa V. Quintana[12], George R. Ricker[2], Pamela Rowden[27], Sara Seager[2,19,22], Paula Sarkis[18], Joshua E. Schlieder[12], Lizhou Sha[2], Andrei Tokovinin[28], Guillermo Torres[1], Roland K. Vanderspek[2], Steven Villanueva, Jr.[2,36], Jesus Noel Villaseñor[2], Joshua N. Winn[15], Bill Wohler[20,25], Ian Wong[19,32], Daniel A. Yahalomi[1], Liang Yu[2], Zhuchang Zhan[19], and George Zhou[1,33]

[1] Center for Astrophysics | Harvard & Smithsonian, 60 Garden Street, Cambridge, MA 02138, USA; joseph.rodriguez@cfa.harvard.edu
[2] Department of Physics and Kavli Institute for Astrophysics and Space Research, Massachusetts Institute of Technology, Cambridge, MA 02139, USA
[3] Department of Astronomy, The University of Texas at Austin, Austin, TX 78712, USA
[4] Department of Physics, The University of Texas at Dallas, 800 West Campbell Road, Richardson, TX 75080-3021 USA
[5] Center of Astro-Engineering UC, Pontificia Universidad Católica de Chile, Av. Vicuña Mackenna 4860, 7820436 Macul, Santiago, Chile
[6] Instituto de Astrofísica, Pontificia Universidad Católica de Chile, Av. Vicuña Mackenna 4860, Macul, Santiago, Chile
[7] Millennium Institute for Astrophysics, Chile
[8] Department of Physics and Astronomy, Vanderbilt University, Nashville, TN 37235, USA
[9] Department of Physics, Fisk University, 1000 17th Avenue North, Nashville, TN 37208, USA
[10] Dunlap Institute for Astronomy and Astrophysics, University of Toronto, Ontario M5S 3H4, Canada
[11] Department of Astronomy, The Ohio State University, 140 West 18th Avenue, Columbus, OH 43210, USA
[12] Exoplanets and Stellar Astrophysics Laboratory, Code 667, NASA Goddard Space Flight Center, Greenbelt, MD 20771, USA
[13] University of Maryland, Baltimore County, 1000 Hilltop Circle, Baltimore, MD 21250, USA
[14] Department of Astronomy and Astrophysics, University of California, Santa Cruz, CA 95064, USA
[15] Department of Astrophysical Sciences, Princeton University, 4 Ivy Lane, Princeton, NJ, 08544, USA
[16] Caltech/IPAC—NASA Exoplanet Science Institute 1200 E. California Avenue, Pasadena, CA 91125, USA
[17] American Association of Variable Star Observers, 49 Bay State Road, Cambridge, MA 02138, USA
[18] Max-Planck-Institut für Astronomie, Königstuhl 17, Heidelberg D-69117, Germany
[19] Department of Earth, Atmospheric and Planetary Sciences, Massachusetts Institute of Technology, Cambridge, MA 02139, USA
[20] NASA Ames Research Center, Moffett Field, CA, 94035, USA
[21] Department of Physics and Astronomy, University of Louisville, Louisville, KY 40292, USA
[22] Department of Aeronautics and Astronautics, MIT, 77 Massachusetts Avenue, Cambridge, MA 02139, USA
[23] Department of Physics and Astronomy, University of North Carolina at Chapel Hill, Chapel Hill, NC 27599, USA
[24] Maury Lewin Astronomical Observatory, Glendora, CA 91741, USA
[25] SETI Institute, Mountain View, CA 94043, USA
[26] Department of Physics, Lehigh University, 16 Memorial Drive East, Bethlehem, PA 18015, USA
[27] School of Physical Sciences, The Open University, Milton Keynes MK7 6AA, UK
[28] Cerro Tololo Inter-American Observatory, Casilla 603, La Serena, Chile

Abstract

We report the discovery of TOI-172 b from the *Transiting Exoplanet Survey Satellite* (*TESS*) mission, a massive hot Jupiter transiting a slightly evolved G star with a 9.48-day orbital period. This is the first planet to be confirmed from analysis of only the *TESS* full frame images, because the host star was not chosen as a two-minute cadence target. From a global analysis of the *TESS* photometry and follow-up observations carried out by the *TESS* Follow-up Observing Program Working Group, TOI-172 (TIC 29857954) is a slightly evolved star with an effective temperature of $T_{\mathrm{eff}} = 5645 \pm 50$ K, a mass of $M_\star = 1.128^{+0.065}_{-0.061}$ $M_\odot$, radius of $R_\star = 1.777^{+0.047}_{-0.044}$ $R_\odot$, a surface gravity of $\log g_\star = 3.993^{+0.027}_{-0.028}$, and an age of $7.4^{+1.6}_{-1.5}$ Gyr. Its planetary companion (TOI-172 b) has a radius of $R_{\mathrm{P}} = 0.965^{+0.032}_{-0.029}$ R_{J}, a mass of $M_{\mathrm{P}} = 5.42^{+0.22}_{-0.20}$ M_{J}, and is on an eccentric orbit ($e = 0.3806^{+0.0093}_{-0.0090}$). TOI-172 b is

[29] Juan Carlos Torres Fellow.
[30] NASA Sagan Fellow.
[31] Kavli Fellow.
[32] 51 Pegasi b Fellow.
[33] NASA Hubble Fellow.
[34] Bernoulli fellow.
[35] Gruber fellow.
[36] Pappalardo Fellow.

one of the few known massive giant planets on a highly eccentric short-period orbit. Future study of the atmosphere of this planet and its system architecture offer opportunities to understand the formation and evolution of similar systems.

Key words: planetary systems – planets and satellites: detection – stars: individual (TIC 29857954)

Supporting material: data behind figure, machine-readable table

1. Introduction

In only three decades, the field of exoplanets has rapidly expanded from its infancy to one of the largest and fastest research areas in astrophysics. This is largely due to the success of both ground-based and space-based efforts to discover new planets using the transit and radial velocity (RV) techniques. With the confirmation of thousands of new planets and the identification of a few thousand more candidates, no survey has been more influential to the field than the *Kepler* mission (Borucki et al. 2010). As the *Kepler* and repurposed *K2* (Howell et al. 2014) missions have completed, we are now entering the next major chapter in the field of exoplanets with the recent launch of the *Transiting Exoplanet Survey Satellite* (*TESS*; Ricker et al. 2015).

Interestingly, we are still attempting to understand one of the first types of planets ever discovered, hot Jupiters. It is commonly believed that close-in giant planets formed farther out in the protoplanetary disk and, through various mechanisms, migrated inward. These highly irradiated, Jovian-sized planets orbit with periods $\leqslant$10 days, and typically do not have nearby planetary companions (Steffen et al. 2012; Huang et al. 2016), suggesting that they might disrupt planet formation and the orbits of any existing inner planets as they move inward. However, the discovery of two small planets bracketing the known hot Jupiter, WASP-47b (Becker et al. 2015), suggests that some giant planets can migrate in a dynamically quiet manner or even form in situ (Batygin et al. 2016; Huang et al. 2016). It has been found that giant planets discovered in more distant orbits tend to have companions (e.g., Knutson et al. 2014; Huang et al. 2016). This possibly supports the idea that their longer orbit allows them to form alongside smaller planets in different parts of the inner disk.

If planetary migration occurs through the gas disk, it must take place during the first ~10 Myr while the gas is still around, and is expected to result in low-eccentricity orbits (Haisch et al. 2001; D'Angelo et al. 2003). However, migration may commonly be influenced by gravitational interactions with other planets or stars. These interactions can increase the planet's orbital eccentricity (known as high eccentricity migration; HEM) and lead to tidal interactions at close approach to the host star that shrink and circularize the orbit (Rasio & Ford 1996; Wu & Murray 2003; Fabrycky & Tremaine 2007; Nagasawa & Ida 2011; Wu & Lithwick 2011). For a Jupiter analog orbiting a Sun-like star on a period of 0.5 to 10 days, the circularization timescale can range from a few million years to over a hundred billion years depending on the semimajor axis (see Equation 2 in Adams & Laughlin 2006). Therefore, only long-period hot Jupiters (5–10 days) would retain any primordial eccentricity if HEM is the underlying mechanism because they would not have had enough time to circularize. This class of dynamically young giant planets, for which the circularization timescales are longer than the system's current age (also referred to as tropical Jupiters; Yu et al. 2018), offers an opportunity to gain insight into the mechanisms governing hot Jupiter evolution. Previous studies have tried to place constraints on hot Jupiter migration mechanisms by analyzing the eccentricities and orbital architectures of these systems. For example, the orbits of dynamically young hot Jupiters tend to be more eccentric on average, as would be expected if at least a fraction of them have undergone eccentric migration (Quinn et al. 2014; Bonomo et al. 2017). At the same time, the paucity of highly eccentric migrating Jupiters places an upper limit on the prevalence of HEM in the production of these systems (Dawson et al. 2015). The presence of additional giant planets exterior to hot Jupiters but inside the ice line is hard to reconcile with migration via HEM (Schlaufman & Winn 2016), though trends with host-star metallicity hint that disk migration and subsequent planet–planet scattering could account for much of the hot Jupiter population (Dawson & Murray-Clay 2013). Indeed, it appears that no single migration channel can produce the known population; a recent review of the relevant literature suggests that the combination of two such mechanisms might be able to explain the observations (Dawson & Johnson 2018). Additional study of the dynamically young planets—and their orbital architectures—can refine our understanding of how these migration mechanisms work together to produce the population of giant planets that we observe.

In this paper, we present the discovery in *TESS* full frame images leading to follow-up photometry, and precision RV measurements of a dynamically young, massive Jupiter in a ~9.5-day eccentric orbit (0.38) around a subgiant. Additionally, the evolutionary state of TOI-172 provides a reliable age. The paper is organized in the following way. We present all available observations of TOI-172 in Section 2 (Table 1 presents the available information on TOI-172 from the literature). Our global analysis of all available observations using EXOFASTv2 is described in Section 3. We discuss TOI-172 b in the context of all known planets in Section 4, presenting prospects on future follow-up. We summarize our conclusions in Section 5.

2. Observations and Archival Data

2.1. TESS *Photometry*

TOI-172 fell on CCD 4 of Camera 1 of the *TESS* spacecraft during its first sector of observations (2018 July 25–August 22), but it was not pre-selected for two-minute cadence observations. After the data were downloaded from the spacecraft, we processed the calibrated 30-minute cadence full frame images (Jenkins et al. 2016) with the MIT Quick Look Pipeline (QLP; C. Huang et al., in preparation). The QLP is a lightweight tool for rapidly producing light curves and identifying transits in *all* stars observed by *TESS*, not just those selected for two-minute cadence observations. The QLP extracts photometry by summing the flux within moving circular apertures (following Huang et al. 2015), after using the nebulosity filter[37] to remove scattered background light from the images. After producing light curves, the QLP searches for

---

[37] Developed by M. Irwin: http://www.ukirt.hawaii.edu/publications/newsletter/ukirtnewsletter2010spring.pdf.

Table 1
Literature and Measured Properties for TOI-172

Other Identifiers			
	TIC 29857954		
	TYC 6932-00301-1		
	2MASS J21063165-2641333		
Parameter	Description	Value	Source
α_{J2000}…	R.A. …	21:06:31.65	1
δ_{J2000}…	decl.…	−26:41:34.29	1
B_T…	Tycho B_T mag.…	12.211 ± 0.203	2
V_T…	Tycho V_T mag.…	11.382 ± 0.125	2
G…	*Gaia* G mag.…	11.193 ± 0.02	3, 4
T…	*TESS* mag.…	10.711 ± 0.019	4
J…	2MASS J mag.…	10.135 ± 0.03	5, 6
H…	2MASS H mag.…	9.825 ± 0.03	5, 6
K_S…	2MASS K_S mag.…	9.722 ± 0.02	5, 6
WISE1…	*WISE1* mag.…	9.673 ± 0.03	7
WISE2…	*WISE2* mag.…	9.718 ± 0.03	7
WISE3…	*WISE3* mag.…	9.763 ± 0.052	7
WISE4…	*WISE4* mag.…	8.529 ± 0.516	7
μ_α…	*Gaia* DR2 proper motion… in R.A. (mas yr^{-1})	−4.711 ± 0.094	3, 4
μ_δ…	*Gaia* DR2 proper motion… in Decl. (mas yr^{-1})	−54.25 ± 0.069	3, 4
$v\sin i_\star$…	Rotational velocity (km s^{-1}) …	5.1 ± 0.5	Section 2.3
[Fe/H]…	Metallicity …	0.14 ± 0.08	Section 2.3
$T_{\rm eff}$…	Effective temperature (K) …	5640 ± 50	Section 2.3
$\log g_\star$…	Surface gravity (cgs)…	3.97 ± 0.1	Section 2.3
π…	*Gaia* parallax (mas) …	2.972 ± 0.06[a]	3, 4
RV…	Systemic radial … velocity (km s^{-1})	−6.247 ± 0.081	Section 2.3
d…	Distance (pc)…	336.47 ± 6.79[a]	3, 4
U[b]…	Space velocity (km s^{-1})…	26.24 ± 0.46	Section 2.7
V…	Space velocity (km s^{-1})…	−71.52 ± 1.68	Section 2.7
W…	Space velocity (km s^{-1})…	−1.31 ± 0.27	Section 2.7

Notes.
[a] Values have been corrected for the $-0.82\,\mu$ as an offset as reported by Stassun & Torres (2018).
[b] U is in the direction of the Galactic center.
References: (1) Cutri et al. (2003); (2) Høg et al. (2000); Gaia Collaboration et al. (2016); (3) Gaia Collaboration et al. (2018); (4) Stassun et al. (2018); (5) Cutri et al. (2003); (6) Skrutskie et al. (2006); (7) Zacharias et al. (2017).

transits by calculating a box-least-squares periodogram (BLS; Kovács et al. 2002), implementing high-pass filtering and BLS period spacing following Vanderburg et al. (2016). We detected a single repeating transit signal around TOI-172 with a period of 9.48 days, a duration of 4.71 hr, and a flat-bottomed shape (see Figure 1). We notified the community of the discovery via the MIT *TESS* alerts portal[38] (Ricker & Vanderspek 2018).

Upon the public release of the processed Sector 1 full frame images, we attempted to improve the light curve by extracting photometry from a variety of differently shaped stationary photometric apertures. After some experimentation, and using archival images from the ESO/SERC Southern Sky Atlas (SERC-J; taken in 1975) and the Anglo-Australian Observatory Second Epoch Survey (AAO-SES; 1993) to check for any additional stars nearby, we settled upon the irregularly

shaped aperture shown in Figure 2. The light curve extracted from this aperture balanced high photometric precision with minimal contamination from a nearby 12th magnitude star (TIC 29857959) and minimal systematics related to *TESS*'s momentum dumps, when the spacecraft thrusters are fired to reorient the spacecraft and allow the reaction wheels to be spun down. We compared the transit depths from the light curve extracted with the QLP and our simple aperture photometry method, and found consistent results. We proceeded in our analysis using the light curve produced with simple aperture photometry, as it had slightly better photometric precision. We manually removed 8 hours of data (BJD$_{\rm TDB}$- 2457000 =1338.4125 to 1338.0792) contaminated by an asteroid passing through the photometric aperture, and we clipped 4σ outliers from the light curve (see Figure 1). The corresponding *TESS* light curve was flattened using a spline fit with breakpoints every 0.5 days to divide out the best-fit stellar variability (Vanderburg & Johnson 2014).

2.2. Ground-based Photometry from the TESS Follow-up Observing Program Working Group

To rule out false positives, better constrain the ephemeris of TOI-172 b, and measure the depth of the transit, we obtained two photometric transit follow-up observations using the Las Cumbres Observatory (LCO) telescope network (Brown et al. 2013).[39] To predict the next possible transit events for TOI-172 that were observable, we used the TAPIR software package (Jensen 2013). We used the AstroImageJ astronomical observation analysis software to reduce all follow-up photometric observations and perform aperture photometry to extract the light curves. On UT 2018 September 22, we observed the transit of TOI-172 b in the Sloan Digital Sky Survey i' filter using the 0.4 m LCO telescope located at the Cerro Tololo Inter-American Observatory (CTIO) in Chile. The 0.4 m telescopes are equipped with SBIG STX6303 cameras that have a $19' \times 29'$ field of view (FOV) and a $0''.57$ pixel scale. On UT 2018 October 11, we observed the transit of TOI-172 b in the z' filter on the 1.0 m telescope at the McDonald Observatory in Fort Davis, Texas. The 1.0 m telescope has a Sinistro camera with a $16'.5 \times 26'.5$ FOV and a pixel scale of $0''.389$ pixel^{-1}. In each case, an ingress of the transit of TOI-172 b was observed on the target star. In both observations, only an ingress was observable and the exposure time was 50 s. These observations are consistent with what was observed by *TESS* (see Figure 3). Therefore, the fading events are localized to within $15''$ of TOI-172.

2.3. Tillinghast Reflector Echelle Spectrograph (TRES) Spectroscopy

Spectra of TOI-172 were obtained on 27 occasions with a resolving power of $R \sim 44000$ using the TRES (Fűrész 2008)[40] mounted on the 1.5 m Tillinghast Reflector at the Fred L. Whipple Observatory (FLWO) on Mt. Hopkins, Arizona. For a description of the reduction and RV extraction pipeline, see Buchhave et al. (2010). Our procedure differed only in the generation of the template used for cross-correlation. We derived relative RVs by cross-correlating against the strongest spectrum, and we shifted and median-combined the spectra to
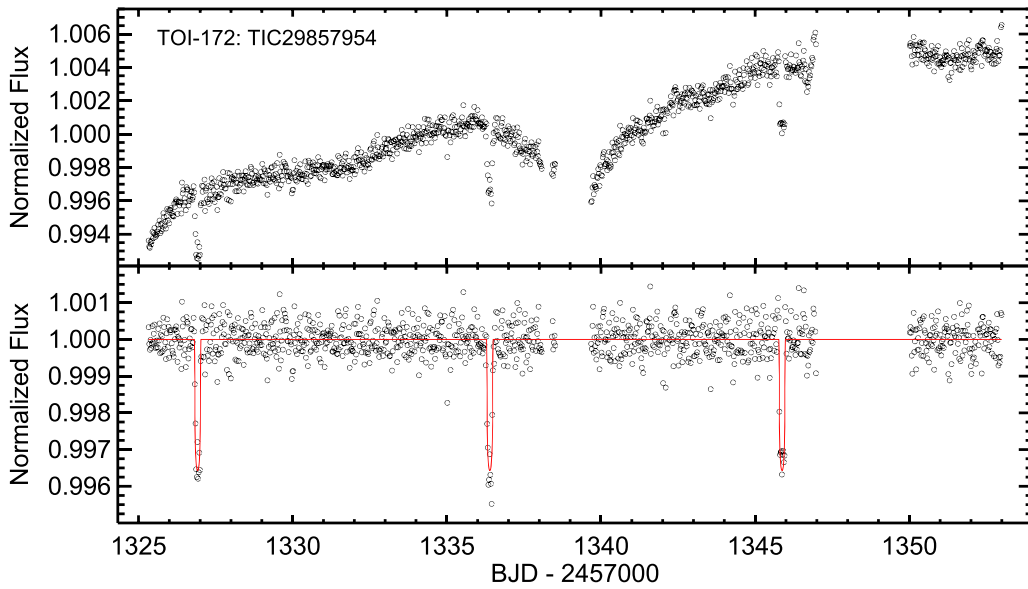
Figure 1. Top: *TESS* 30-minute cadence light curve of TOI-172. Bottom: the flattened final *TESS* light curve used in the EXOFASTv2 fit. The observations are plotted in open black circles, and the best-fit model from EXOFASTv2 is plotted in red. The gap in the middle is due to the gap between *TESS* orbits. The data between BJD_{TDB}- 2457000 of 1347 to 1350 were removed due to high scatter caused when the spacecraft thrusters are fired to reorient the spacecraft and allow the reaction wheels to spin down. There is also a small 8 hr gap on BJD_{TDB}- 2457000 = 1338 due to an asteroid crossing the aperture for TOI-172. The data used to create this figure are available.
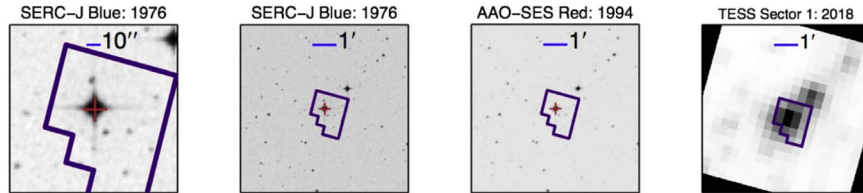
Figure 2. Archival imaging of TOI-172 from the ESO/SERC Southern Sky Atlas (SERC-J; taken in 1976, first and second panels) and the Anglo-Australian Observatory Second Epoch Survey (AAO-SES; 1994, 3rd panel). Fourth panel: the *TESS* image of TOI-172 from Sector 1. The outline on each image corresponds to the final chosen aperture used to extract the *TESS* light curve and the blue horizontal bar shows the image scale.
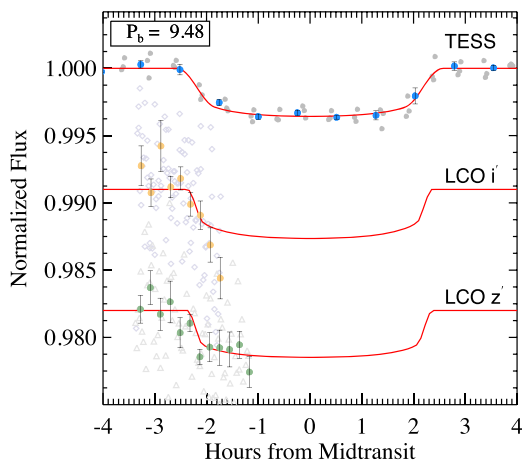
Figure 3. Phase-folded corrected *TESS* (blue), LCO i′ (yellow), and LCO z′ (green) light curves for TOI-172 b. The full light curves are shown with filled circles (*TESS*), open diamonds (LCO i′), and open triangles (LCO z′), and the binned points are shown in color with error bars. The bin sizes are 45 minutes for *TESS* and 11 minutes for the LCO observations. The red line corresponds to the final EXOFASTv2 transit model.

produce a high signal-to-noise ratio template spectrum. We then cross-correlated each observed spectrum against that template to produce our final relative RVs, which are given in Table 2 and shown in Figure 4. Bisector spans were calculated

for the TRES RVs using the technique described in Torres et al. (2007). There are no correlations between the bisector spans and the measured RV values and no scatter in the bisectors beyond their uncertainties (which are small compared to the RV variation), supporting the premise that TOI-172 is being periodically transited or eclipsed. We also derive the absolute RVs via cross-correlation against synthetic templates created using Kurucz model atmospheres (Kurucz 1992). We calculate the instrumental zero-point through nightly monitoring of RV standards, which we place on the absolute RV scale of Nidever et al. (2002). Using these observations, we determine the absolute center-of-mass velocity of TOI-172 to be −6.247 ± 0.081 km s^{-1}(consistent with the absolute RV from *Gaia* DR2 of −5.89 ± 0.67).

To determine the stellar parameters of TOI-172, we analyzed the TRES spectra using the stellar parameter classification (SPC) analysis package (Buchhave et al. 2012). From this analysis, we estimated the effective temperature, metallicity, surface gravity, and rotational velocity of TOI-172 to be T_{eff} =5640 ± 50 K, $\log g_{\star} = 3.97 \pm 0.1$, $[m/H] = 0.14 \pm 0.08$, and $v \sin I_{\star} = 5.1 \pm 0.5$ km s^{-1}. We use the T_{eff} and [Fe/H] as a prior in the EXOFASTv2 global fit (see Section 3).

2.4. FEROS Spectroscopy

We also obtained nine R = 48000 spectra of TOI-172 between UT 2018 October 19 and November 5 using the

Table 2
Relative Radial Velocities for TOI-172

BJD$_{\rm TDB}$	RV (m s^{-1})	σ_{RV} (m s^{-1})	Bisectors	Instrument
2458410.551705	−5716.4	7.4	−1.0 ± 10.0	FEROS
2458411.636884	−5739.9	9.9	6.0 ± 13.0	FEROS
2458415.573206	−6562.4	8.6	−4.0 ± 11.0	FEROS
2458418.552974	−6100.9	7.1	−18.0 ± 10.0	FEROS
2458419.511487	−5865.5	7.9	38.0 ± 11.0	FEROS
2458423.625864	−6654.1	8.3	−15.0 ± 11.0	FEROS
2458424.531225	−6584.4	7.0	8.0 ± 10.0	FEROS
2458425.597896	−6474.7	7.8	−7.0 ± 11.0	FEROS
2458427.583262	−6149.8	7.4	−8.0 ± 10.0	FEROS
2458429.542763	−5682.3	7.4	13.0 ± 10.0	FEROS
2458430.614729	−5660.9	17.1	35.0 ± 19.0	FEROS
2458376.730770	−593.6	27.0	13.3 ± 19.0	TRES
2458390.710107	122.0	17.6	7.5 ± 14.7	TRES
2458397.687254	−359.0	14.0	23.7 ± 21.2	TRES
2458398.649461	−206.5	26.2	16.5 ± 18.4	TRES
2458400.688662	230.9	22.4	8.5 ± 21.9	TRES
2458409.670769	78.7	35.8	−56.7 ± 33.4	TRES
2458413.668975	−569.8	43.0	−123.3 ± 51.7	TRES
2458415.631951	−499.7	21.2	−5.3 ± 22.6	TRES
2458416.639897	−373.8	30.9	13.6 ± 29.0	TRES
2458417.601186	−194.6	23.1	1.0 ± 21.6	TRES
2458418.659549	−8.6	24.7	14.1 ± 28.5	TRES
2458419.685623	274.1	23.1	−10.4 ± 35.5	TRES
2458420.614450	422.1	20.0	16.4 ± 16.1	TRES
2458423.681839	−559.6	46.0	−9.8 ± 23.3	TRES
2458424.653259	−520.3	26.9	25.1 ± 25.3	TRES
2458426.597813	−250.4	22.6	10.5 ± 25.6	TRES
2458428.594704	126.1	16.5	29.0 ± 15.2	TRES
2458430.627687	291.2	19.2	37.342 ± 2.3	TRES
2458438.602799	228.7	16.3	25.6 ± 11.2	TRES
2458439.594972	403.1	16.6	−3.7 ± 11.5	TRES
2458440.586306	−29.0	12.8	1.5 ± 13.9	TRES
2458441.577056	−528.6	15.8	30.8 ± 13.1	TRES
2458442.582383	−617.8	13.8	21.4 ± 14.7	TRES
2458443.586964	−548.2	19.5	−15.5 ± 22.6	TRES
2458444.630963	−471.7	39.9	−67.3 ± 45.2	TRES
2458446.575996	−135.6	18.0	−33.4 ± 18.1	TRES
2458447.572304	104.0	15.1	29.4 ± 15.9	TRES

(This table is available in machine-readable form.)

Fiber-fed Extended Range Optical Spectrograph (FEROS; Kaufer et al. 1999) mounted on the 2.2 m Max Planck Gesellschaft (MPG) telescope at La Silla observatory in Chile. Each spectrum achieved a signal-to-noise ratio of ~60–100 per spectral resolution element with exposure times of 600 s. The instrumental drift was determined via comparison with a simultaneous fiber illuminated with a ThAr+Ne lamp. The data were processed with the CERES suite of echelle pipelines (Brahm et al. 2017), which produce RVs and bisector spans in addition to reduced spectra.

2.5. High-resolution Imaging

The relatively large 21″ pixels of *TESS* can result in photometric contamination from nearby sources. These must be accounted for to help rule out astrophysical false positives, such as background eclipsing binaries, and to correct the estimated planetary radius, initially derived from the diluted transit in a blended light curve (Ciardi et al. 2015; Ziegler et al. 2018). We searched for close companions to TOI-172 with speckle imaging on the 4.1 m Southern Astrophysical Research (SOAR) telescope (Tokovinin 2018) on UT 2018 September 25, and again in better conditions on UT 2018 October 21. We also obtained adaptive optics (AO) images of the target on UT 2018 November 14 using Gemini/NIRI. For these observations, nine science frames with an exposure time of 11 s each were collected, with the telescope dithered between each frame. For a subset of the frames, the raw data showed signs of stripping, and so we discarded these frames and combined only the six good frames for the analysis. We flat-field and sky subtract the frames, using a sky background constructed by median combining the dithered images, and then align and combine the images. Figure 5 shows the 5σ detection limits along with the AO image and speckle autocorrelation function.

A nearby star was detected in both the speckle and the AO observations. The object is measured at a separation of 1″104 and an *I*-band contrast of 4.9 mag in the speckle images, and at a separation of 1″099 and a Brγ contrast of 4.5 mag in the AO images. This would result in a 371 au projected separation if the companion is at the same distance as TOI-172. To test this
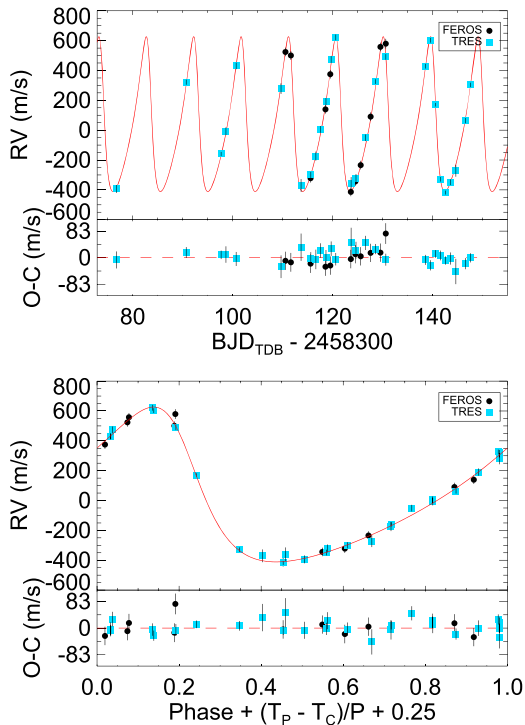
Figure 4. Top: RV measurements from FEROS (black) and TRES (blue). Bottom: the RV measurements are phase-folded to the best determined period by EXOFASTv2, 9.477 days. The EXOFASTv2 model is shown in red and the residuals to the best fit are shown below each plot.

assumption, we use the broadband photometry in these two bands for TOI-172 (2MASS $K_s = 9.722$ and USNO $I' = 10.50$; Monet et al. 2003) and the measured contrasts for the companion ($\Delta Br\gamma = 4.5$ and $\Delta I = 4.9$) to derive the $I - K_s$ colors to be 0.78 and 1.18, respectively. Using these colors and the MESA Isochrones and Stellar Tracks (MIST) stellar evolution models (Paxton et al. 2011, 2013, 2015; Choi et al. 2016; Dotter 2016) at a log(age) = 9.9 and a solar metallicity (the nearest isochrone grid for TOI-172), we estimate a photometric distance to TOI-172 to be 318 pc. This is in close agreement with the *Gaia* distance (336.47 pc). However, assuming that the companion is on the main sequence, we estimate its distance to be 1092 pc. When using other MIST isochrone grids near the one adopted here, we only see a small change in the derived photometric distances, not nearly enough to explain the large difference measured between TOI-172 and the visual companion. This discrepancy suggests that the visual companion is likely a background object, and not gravitationally bound to the planet host. More data are required to confirm this conclusion, either in the form of more photometry to further characterize the spectral energy distribution (SED) of the visual companion, or additional astrometric measurements that confirm whether the two stars share common proper motion.

The nearby star is not in *Gaia* DR2 or the *TESS* input catalog (TIC), and consequently was not accounted for in the contamination correction for TOI-172. It would take a 28.5% deep eclipse of the nearby faint companion to cause the blended depth seen in our aperture for TOI-172. The high contrast between the two stars significantly reduces the possibility that the nearby star is a background eclipsing binary resulting in a false-positive planetary transit signal, as does subsequent RV follow-up. We know that such a faint

companion is unable to significantly affect the RVs of TOI-172 because its contribution to the line profile is so small. While it is true that even a faint companion could affect the RVs slightly (even if it is below the noise level of the cross-correlation function, CCF), this would only be at the level of $m\,s^{-1}$, not hundreds of $m\,s^{-1}$ (TOI-172b $k = 517\,m\,s^{-1}$, see the analysis of blended CCFs in Buchhave et al. 2011). Therefore, the spectroscopy proves that the planetary companion orbits our target. Assuming the primary star is the planet host, the additional flux from the nearby star results in only a negligible correction upwards to the initially derived planet radius ($\sim$0.5%). We account for the blending from this nearby companion in our global fit (see Section 3).

2.6. SED Analysis

Due to the presence of a nearby visual companion (see Figure 5), we are unable to simultaneously fit the SED within the EXOFASTv2 global analysis. Instead, we fit the combined SED of the two stars separately from the joint transit and RV analysis. The companion is blended in each of the broadband photometric observations. From our analysis of the speckle high-resolution imaging, we know that the nearby companion has an I-band contrast of 4.9 mag and a $Br\gamma$ contrast of 4.5 mag. Using the available photometric observations (see Table 1), we fit the broadband SED of TOI-172 spanning 0.2–20 μm (Figure 6). Assuming both stars have the same A_V, we use the ΔI and $\Delta Br\gamma$ contrasts to fit an SED to the nearby companion. Each flux measurement is fit using the stellar atmosphere models of Kurucz (1992). The distance for TOI-172 is adopted from the measured *Gaia* parallax and we use the SPC determined T_{eff}, $\log g_\star$, and [Fe/H] as Gaussian priors on the fit. The only free parameter is the extinction (A_V) which is constrained at its upper bound by the maximum permitted line-of-sight extinction from Schlegel et al. (1998). Our final best-fit SED for TOI-172 has a reduced χ^2 of 1.7, an extinction of $A_V = 0.08 \pm 0.04$, and is shown in Figure 6. We integrated the best-fit SED to determine the unextincted bolometric flux (correcting for the contamination of the companion) received at Earth, $F_{bol} = 8.16 \pm 0.19 \times 10^{-10}\,erg\,s^{-1}\,cm^{-2}$. Using the *Gaia* parallax (corrected for the systematic offset reported by Stassun & Torres 2018) combined with the adopted T_{eff} from this analysis, we are able to measure the radius of TOI-172 to be $R_\star = 1.787 \pm 0.049\,R_\odot$, after accounting for the presence of the nearby companion seen in our high-resolution imaging. We use this determined $R_\star$ as a prior for the EXOFASTv2 global analysis (see Section 3). Using our two-component SED fit, we determine the flux contribution of the nearby companion to be 0.91%(*TESS*), 0.46% (g'), and 1.07% (z'). We note that the contribution from the companion would correspond to a change in the measured *TESS* transit depth $<1\sigma$.

2.7. Location in the Galaxy, UVW Space Motion, and Galactic Population

TOI-172 is located at $\alpha_{J2000} = 21^h06^m31\overset{s}{.}65$ and $\delta_{J2000} = -26°41'34\overset{''}{.}29$, and from *Gaia* DR2 the parallax is 2.89 ± 0.06 mas (applying the correction from Stassun & Torres 2018), corresponding to a distance of 336.47 ± 6.79 pc ignoring the Lutz–Kelker bias, which can cause measured parallaxes to be larger than they are due to the assumption that the number of observable stars increases as you go farther out (Lutz & Kelker 1973). This results in TOI-172 being 217.6 pc below the
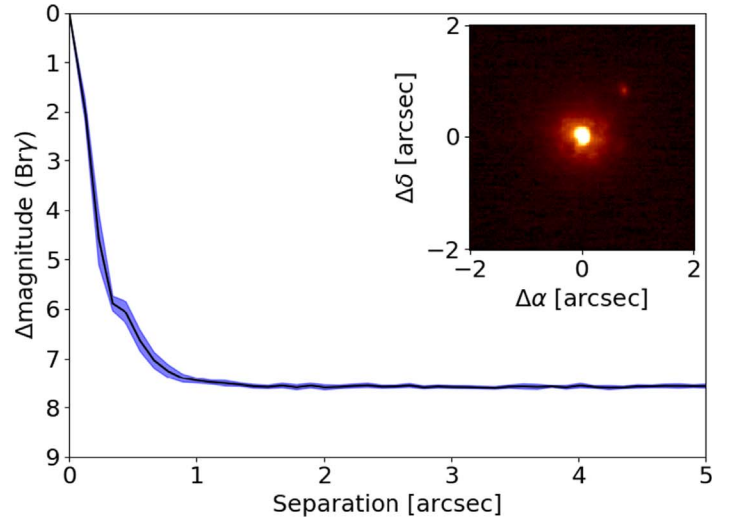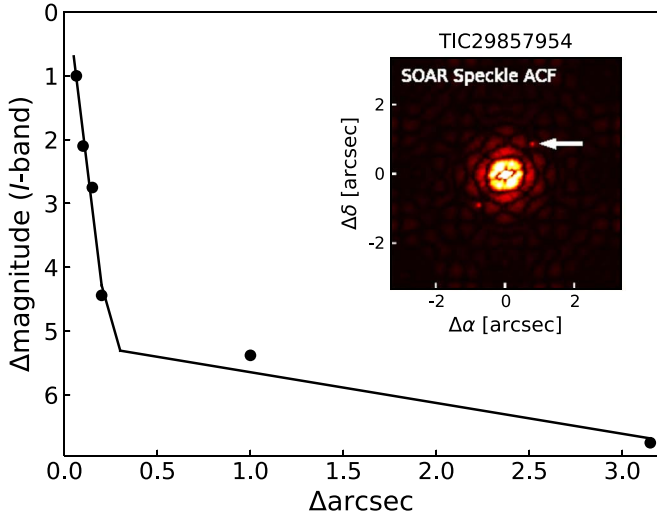
Figure 5. Left: the *I*-band autocorrelation function from speckle using SOAR. The 5σ contrast curve for TOI-172 is shown by the black points. The black solid line is the linear fit to the data for separations $<0\rlap{.}''2$ and $>0\rlap{.}''2$. The autocorrelation function is shown within the contrast curve plot. Right: the Brγ-band AO image and 5σ contrast curve for TOI-172. The faint companion is detected in both data sets; in the speckle autocorrelation function (ACF), the white arrow points to the position of the visual companion, which is mirrored in the ACF by the speckle processing.
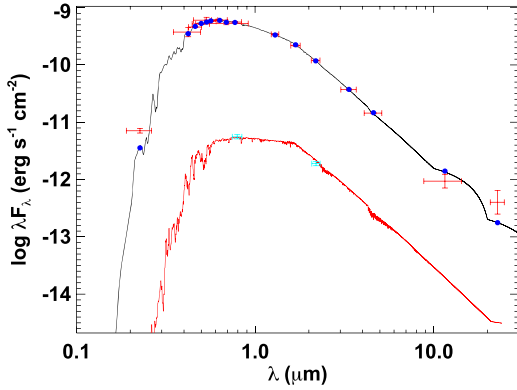
Figure 6. Two-component SED fit for TOI-172. The blue points are the predicted integrated fluxes and the red points are the observed values at the corresponding passbands. The cyan points correspond to the *I*-band flux of the nearby companion observed by SOAR (ΔI-band) and the Brγ flux observed by Gemini. The width of the bandpasses are the horizontal red error bars and the vertical errors represent the 1σ uncertainties. The final model fit is shown by the solid line for TOI-172 (black) and its companion (red).

Galactic plane. Combining the *Gaia* DR2 proper motions of $(\mu_\alpha, \mu_\delta) = (-4.711 \pm 0.094, -54.25 \pm 0.069)$ mas yr^{-1}, the *Gaia* parallax, and the absolute RV as determined from the TRES spectroscopy of -6.25 ± 0.081 km s^{-1}, we determine the three-dimensional Galactic space motion of $(U, V, W) = (26.24 \pm 0.46, -71.52 \pm 1.68, -1.31 \pm 0.27)$ km s^{-1}, where positive U is in the direction of the Galactic center. We adopt the Coşkunoğlu et al. (2011) determination of the solar motion with respect to the local standard of rest. The large asymmetric drift (large negative *V* velocity) of the host star, combined with its relatively large vertical height below the plane, suggests that the star could potentially be a member of the thick disk. Indeed, TOI-172 has a 43.9% chance of being in the thin disk according to the classification scheme of Bensby et al. (2003). However, this conclusion is somewhat contraindicated by the slightly super-solar metallicity of the host star. We suggest a measurement of the star's detailed elemental abundances (in

particular $[\alpha/\text{Fe}]$) could clarify the Galactic population to which this star belongs.

3. EXOFASTv2 Global Fit for TOI-172

We use the EXOFASTv2 modeling suite (Eastman et al. 2013; Eastman 2017) to perform a simultaneous fit of the available photometric and spectroscopic observations to gain a full understanding of the TOI-172 system. EXOFASTv2 is heavily based on the original EXOFAST modeling suite (Eastman et al. 2013) but provides flexibility in allowing the user to simultaneously fit the SED, RV observations from multiple instruments, and an arbitrary number of planets. We simultaneously fit the full frame image *TESS* light curve (see Section 2.1 and Figure 1), accounting for the effect of the 30-minute cadence smearing on the light curve, the follow-up ingresses observed by LCO, and the RV observations from TRES and FEROS (see Figure 4). From our speckle observations and two-component SED analysis, we found that the nearby companion $1\rlap{.}''1$ from TOI-172 contributes 0.91%, 0.46%, and 1.07% of the total flux of the system in the *TESS*, g', and z' bandpasses. To properly deblend the *TESS* and follow-up observations from the previously unknown companion, we include these flux contributions with a 5% error as Gaussian priors in the EXOFASTv2 global fit. This error has no influence on the determined results.

Because accurate *TESS* pixel response function (PRF) models are not yet available, we did not attempt to deblend the *TESS* light curve from contaminating flux from TIC 29857959, the 12th magnitude star 75 arcsec northwest of TOI-172 (see the discussion of this object in Section 2.1 and Figure 2). We did, however, confirm that the neighbor's contaminating flux does not significantly dilute the transit depth of TOI-172 b using several methods. First, we extracted the light curve of TOI-172 from even smaller apertures than the one shown in Figure 2, and found that decreasing the aperture size had no effect on the depths of the transits (empirically showing dilution is not an important factor). We also estimated the local *TESS* PRF by examining *TESS* images of the nearby

Table 3
Median Values and the 68% Confidence Interval for the Global Model of
TOI-172

Parameter	Units	Values
Stellar Parameters		
M_*…	Mass ($M_\odot$)…	$1.128^{+0.065}_{-0.061}$
R_*…	Radius ($R_\odot$)…	$1.777^{+0.047}_{-0.044}$
L_*…	Luminosity ($L_\odot$)…	$2.89^{+0.19}_{-0.18}$
ρ_*…	Density (cgs)…	$0.286^{+0.022}_{-0.023}$
$\log g$…	Surface gravity (cgs)…	$3.993^{+0.027}_{-0.028}$
T_{eff}…	Effective temperature (K)…	5645 ± 50
[Fe/H]…	Metallicity (dex)…	$0.148^{+0.079}_{-0.080}$
[Fe/H]$_0$[a]…	Initial metallicity …	$0.172^{+0.074}_{-0.078}$
Age…	Age (Gyr)…	$7.4^{+1.6}_{-1.5}$
EEP[b]…	Equal evolutionary point …	$456.0^{+3.5}_{-6.8}$

Notes.
[a] The initial metallicity is the metallicity of the star when it was formed.
[b] The equal evolutionary point (EEP) corresponds to static points in a stars evolutionary history when using the MIST isochrones and can be a proxy for age. See Section 2 in Dotter (2016) for a more detailed description of EEP.

isolated bright star (TIC 29857846). Inspection of these images showed that in this region of the *TESS* FOV, about 75% of the total flux falls within one pixel of the peak of the PRF, and virtually all of the flux falls within about six pixels of the peak. The photometric aperture for TOI-172 covers about 10% of the detector area within six pixels of TIC 29857959, so only about 2.5% of the neighboring star's total flux contaminates TOI-172's aperture. Since TIC 29857959 is about 1.3 magnitudes fainter than TOI-172, the contamination from TIC 29857959 should only be about 1% the total flux in the aperture, much smaller than the uncertainties on the depth of the transit, and therefore negligible for the transit fitting.[41] Finally, we note that this estimate of about 1% contamination from TIC 29857959 is consistent with the contamination estimated by version 7 of the TIC using pre-launch estimates of the PRF.

To characterize the host star within the fit, we use the MIST stellar evolution models (Paxton et al. 2011, 2013, 2015; Choi et al. 2016; Dotter 2016). We enforce Gaussian priors on T_{eff} (5640 ± 50 K) and [Fe/H] (0.14 ± 0.08) from the SPC analysis of the TRES spectra (see Section 2.3). We also place a Gaussian prior on R_* of $1.783 \pm 0.049\,R_\odot$ from the two-component SED analysis that included the *Gaia* DR2 parallax (see Section 2.6). The final determined system parameters for TOI-172 are shown in Tables 3 and 4. Our determined $R_\star$ is larger than what was listed in the TIC because version 7 of the TIC did not have a *Gaia* parallax for TOI-172 and relied on color relations that are unable to distinguish between dwarfs and subgiants.

4. Discussion

Our global analysis indicates that TOI-172 has interesting characteristics that warrant further study. Specifically, TOI-172 b is now one of only four known planets that has a highly eccentric orbit (>0.3), a high planetary mass ($>3\,M_J$), relatively short period (<20 days), and is bright enough ($V<12$) to be well suited for atmospheric characterization.[42]

The host star has a mass of $M_\star = 1.128^{+0.065}_{-0.061}\,M_\odot$, a radius of $R_\star = 1.777^{+0.047}_{-0.044}$, a surface gravity of $\log g_\star = 3.993^{+0.027}_{-0.028}$, and an age of $7.4^{+1.6}_{-1.5}$ Gyr. Therefore, TOI-172 appears to have just evolved off the main sequence and to be entering into the relatively short subgiant phase (see Figure 7).

4.1. Tidal Evolution and Irradiation History

To gain a better understanding of the past and future evolution of TOI-172 b's orbit, we use the latest version of POET,[43] where the results of our EXOFASTv2 global analysis (see Section 3) are used as boundary conditions. POET is a tool for calculating the evolution of a planetary orbit (circular aligned) as a result of tidal dissipation (see Penev et al. 2014 for a detailed description of the original version of POET). Here we present an overview of the major changes that were used for the analysis of TOI-172 b. The current version allows for inclined and eccentric orbits, where either object in the binary system can be a star or a planet. For the purposes of TOI-172, the difference between a star and a planet is that stars evolve (e.g., their radius changes) while planets do not. We assume that the star follows the MIST evolutionary tracks used in the EXOFASTv2 global model and that the rotation period of TOI-172 is always longer than the orbital period of the planet. We note that this is not strictly true, since stars similar to TOI-172 typically have a rotation period less than ∼9.5 days earlier in their lifetime while they are on the main sequence. This assumption only affects the very early part of the analysis (near a zero-age main sequence), since the part of the evolution after the star has started spinning slower than the orbit is determined entirely by the present state of the system. We note that the estimated $v\sin I_\star$ from the TRES spectroscopy suggests a maximum rotation period of 17.6 days.

For TOI-172, orbital evolutionary tracks were calculated for $Q^\star = 10^6$, 10^7, and 10^8, and for each of those, $Q_P = 10^6$, 10^7, and 10^8 (see Figure 8). The tidal quality factor (Q) defines the efficiency of tidal dissipation within the planet or star. Each track uses initial conditions that reproduce the present-day orbital period and eccentricity of the system. Unfortunately, due to the high density of the planet and its relatively large semimajor axis, we are unable to produce meaningful constraints on Q_P or $Q^\star$ (see Figure 8). In particular, even for $Q^\star = 10^6$ and $Q_P = 10^6$ the amount of circularization this system has undergone is relatively low. When using $Q^\star = 10^5$, we are not able to find an initial eccentricity large enough to replicate the present eccentricity observed for TOI-172 b. However, we are unable to try initial eccentricities larger than about $e = 0.6$, because the Taylor series expansion of the tidal potential in eccentricity diverges past that point.

This system contradicts normal conventional wisdom that tidal circularization is dominated by tides raised on the planet since the rate of circularization scales as $(M'/M) \times R^5$, where M and R are the mass and radius of the body experiencing the tides, and M' is the mass of the companion (Adams & Laughlin 2006). For a typical Jupiter mass planet around a Solar-type star, the contribution from tides raised on the planet is stronger than that from tides raised on the star by a factor of 10. However, TOI-172 b is more massive than Jupiter ($M_P = 5.4\,M_J$) and the host star is larger than the Sun ($R_\star = 1.78\,R_\odot$). Compared to the fiducial case, these contribute

---

[41] The uncertainty on the transit depth is about 4%, so 1% dilution affects the measured depth by much less than 1σ.
[42] https://exoplanetarchive.ipac.caltech.edu/; Akeson et al. (2013).
[43] https://github.com/kpenev/poet

Table 4
Median Values and the 68% Confidence Interval for the Global Model of TOI-172

Parameter	Description (Units)	Values		
P…	Period (days)…	$9.47725^{+0.00064}_{-0.00079}$		
R_P…	Radius (R_J)…	$0.965^{+0.032}_{-0.029}$		
T_C…	Time of conjunction (BJD_{TDB})…	2458326.9190 ± 0.0017		
T_0[a]…	Optimal conjunction Time (BJD_{TDB})…	2458345.8734 ± 0.0013		
a…	Semimajor axis (au)…	0.0914 ± 0.0017		
i…	Inclination (Degrees)…	$88.2^{+1.1}_{-1.0}$		
e…	Eccentricity …	$0.3806^{+0.0093}_{-0.0090}$		
ω_*…	Argument of Periastron (Degrees)…	57.1 ± 1.7		
T_{eq}…	Equilibrium temperature (K)…	1198^{+18}_{-17}		
M_P…	Mass (M_J)…	$5.42^{+0.22}_{-0.20}$		
K…	RV semi-amplitude (m s^{-1})…	517.6 ± 6.2		
$\log K$…	Log of RV semi-amplitude …	2.7140 ± 0.0052		
R_P/R_*…	Radius of planet in stellar radii …	$0.05588^{+0.00091}_{-0.00092}$		
a/R_*…	Semimajor axis in stellar radii …	$11.09^{+0.28}_{-0.30}$		
δ…	Transit depth (fraction)…	0.00312 ± 0.00010		
Depth…	Flux decrement at mid transit …	0.00312 ± 0.00010		
τ…	Ingress/egress transit duration (days)…	$0.01093^{+0.00085}_{-0.00050}$		
T_{14}…	Total transit duration (days)…	$0.1964^{+0.0028}_{-0.0029}$		
T_{FWHM}…	FWHM transit duration (days)…	0.1853 ± 0.0029		
b…	Transit Impact parameter …	$0.22^{+0.12}_{-0.14}$		
b_S…	Eclipse impact parameter …	$0.43^{+0.23}_{-0.27}$		
τ_S…	Ingress/egress eclipse duration (days)…	$0.0229^{+0.0054}_{-0.0024}$		
$T_{S,14}$…	Total eclipse duration (days)…	$0.355^{+0.026}_{-0.043}$		
$T_{S,FWHM}$…	FWHM eclipse duration (days)…	$0.332^{+0.027}_{-0.048}$		
$\delta_{S,3.6\,\mu m}$…	Blackbody eclipse depth at 3.6 μm (ppm)…	$115.2^{+7.8}_{-6.3}$		
$\delta_{S,4.5\,\mu m}$…	Blackbody eclipse depth at 4.5 μm (ppm)…	$176.7^{+10.}_{-8.6}$		
ρ_P…	Density (cgs)…	$7.53^{+0.65}_{-0.72}$		
$\log g_P$…	Surface gravity …	$4.162^{+0.026}_{-0.031}$		
Θ…	Safronov number …	$0.908^{+0.030}_{-0.031}$		
$\langle F \rangle$…	Incident flux (10^9 erg s^{-1} cm^{-2})…	$0.407^{+0.026}_{-0.022}$		
T_P…	Time of Periastron (BJD_{TDB})…	$2458326.549^{+0.025}_{-0.027}$		
T_S…	Time of eclipse (BJD_{TDB})…	$2458323.485^{+0.052}_{-0.049}$		
T_A…	Time of ascending node (BJD_{TDB})…	$2458325.863^{+0.025}_{-0.024}$		
T_D…	Time of descending node (BJD_{TDB})…	$2458328.667^{+0.050}_{-0.049}$		
$e\cos\omega_*$…	…	$0.2065^{+0.0086}_{-0.0082}$		
$e\sin\omega_*$…	…	0.319 ± 0.012		
$M_P \sin i$…	Minimum mass (M_J)…	$5.42^{+0.22}_{-0.21}$		
M_P/M_*…	Mass ratio …	$0.004587^{+0.000100}_{-0.00011}$		
d/R_*…	Separation at mid transit …	$7.17^{+0.24}_{-0.23}$		
P_T…	A priori non-grazing transit prob …	$0.1316^{+0.0044}_{-0.0043}$		
$P_{T,G}$…	A priori transit prob …	$0.1472^{+0.0050}_{-0.0048}$		
P_S…	A priori non-grazing eclipse prob …	$0.0677^{+0.0020}_{-0.0016}$		
$P_{S,G}$…	A priori eclipse prob …	$0.0757^{+0.0023}_{-0.0018}$		
Wavelength Parameters		i'	z'	*TESS*
u_1…	linear limb-darkening coeff …	0.325 ± 0.051	0.263 ± 0.050	0.310 ± 0.049
u_2…	quadratic limb-darkening coeff …	$0.271^{+0.050}_{-0.051}$	$0.270^{+0.049}_{-0.050}$	$0.263^{+0.049}_{-0.050}$
A_D…	Dilution from neighboring stars …	$0.0017734^{+0.0000063}_{-0.0000062}$	0.014331 ± 0.000051	0.007830 ± 0.000028
Telescope Parameters		FEROS	TRES	
γ_{rel}…	Relative RV offset (m s^{-1})…	$-6240.2^{+10.}_{-9.5}$	-195.7 ± 4.2	
σ_J…	RV jitter (m s^{-1})…	$30.0^{+12}_{-8.4}$	$6.4^{+7.7}_{-6.4}$	
σ_J^2…	RV jitter variance …	900^{+900}_{-430}	41^{+160}_{-95}	
Transit Parameters		LCO UT 2018-09-22 (i')	LCO UT 2018-10-11 (z')	*TESS*
σ^2…	Added variance …	$0.0000192^{+0.0000030}_{-0.0000025}$	$0.0000085^{+0.0000016}_{-0.0000013}$	$-0.0000000139^{+0.0000000083}_{-0.0000000078}$
F_0…	Baseline flux …	1.00051 ± 0.00046	$0.99970^{+0.00038}_{-0.00037}$	1.000007 ± 0.000013

Note.
[a] Minimum covariance with period. All values in this table for the secondary occultation of TOI-172 b are predicted values from our global analysis.
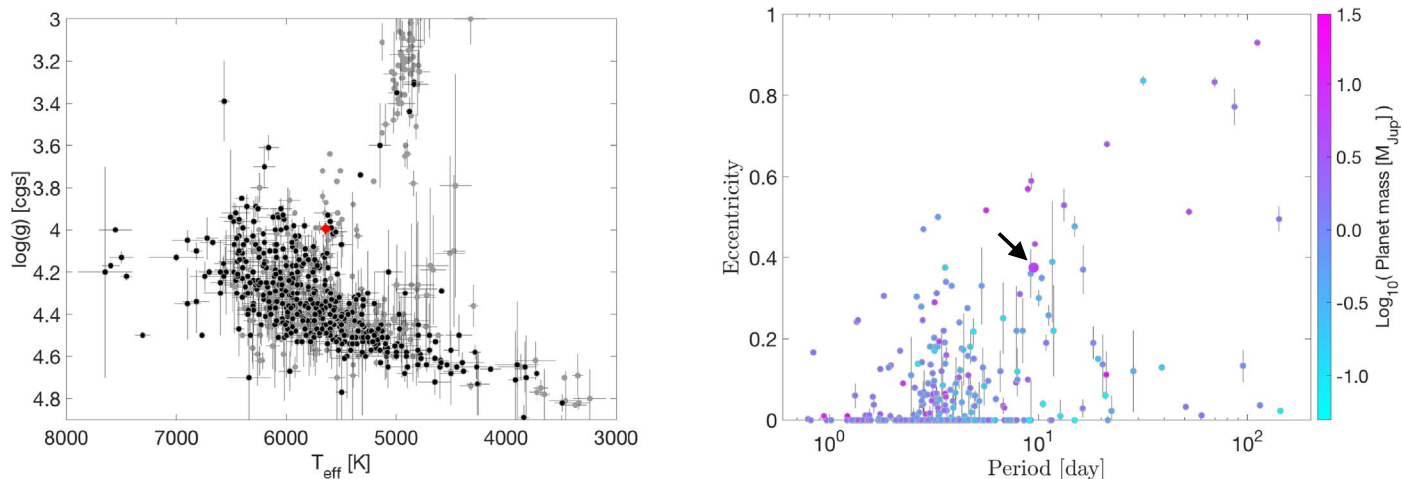
Figure 7. Left: log g and $T_{\rm eff}$ of all known stars with transiting (black) and RV (gray) discovered exoplanets. TOI-172 b is shown in red. Right: period and eccentricity of all known exoplanets color coded by $\log(M_P)$. TOI-172 b is identified by the larger data point and the black arrow. The data behind these figures were downloaded on UT 2018 December 21 from the NASA Exoplanet Archive (Akeson et al. 2013).
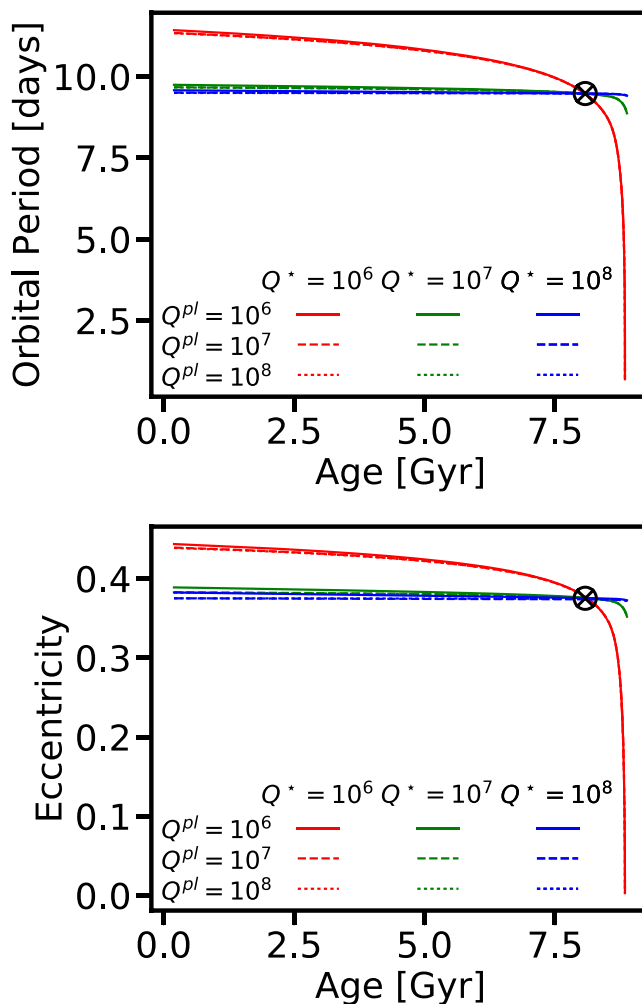
Figure 8. Evolution of the (top) orbital period and (bottom) eccentricity for TOI-172 b shown for a range of values for $Q^\star$. The color of the line indicates the dissipation in the star (red: $Q^\star = 10^6$, green: $Q^\star = 10^7$, blue: $Q^\star = 10^8$) and the line style indicates the dissipation in the planet (solid: $Q_P = 10^6$, dashed: $Q_P = 10^7$, and dotted: $Q_P = 10^8$). The tidal circularization in this system is dominated by tides raised on the star, rather than the planet (see Section 4.1).

to an increase by a factor of nearly 90 in the rate of circularization due to tides raised on the star and a decrease by a factor of about 7 in the rate of circularization due to tides raised on the planet. Therefore, the present-day orbital evolution of TOI-172 b is dominated by the tides raised on its host star by the planet.

4.2. Atmospheric Characterization Prospects

The high eccentricity observed in the planet's orbit combined with the slight evolution of the host star make TOI-172 b an interesting target for detailed characterization. While it is possible that hot Jupiters form in situ (Batygin et al. 2016), most formation theories suggest that these planets form at larger distances from their host stars (core accretion or gravitational instability; Pollack et al. 1996; Boss 2000; Gammie 2001; Lissauer & Stevenson 2007; Boley 2009) and migrate inward via two main interactions, either with drag due to the original protoplanetary disk during formation or by gravitational interaction with another body in the system (Rasio & Ford 1996; Fabrycky & Tremaine 2007; Papaloizou et al. 2007). It was originally believed that the large number of hot Jupiters shown to have misaligned orbits relative to the host star's spin axis indicated that these systems must migrate through gravitational scattering (Winn et al. 2010). However, the origin of these misalignments could have occurred from misalignments in the protoplanetary disk (Batygin 2012; Crida & Batygin 2014). Therefore, it is unclear what migration mechanism is responsible for close-in Jovian planets.

The migration mechanism may be revealed by studying the chemical abundances in the planet's atmosphere. Specifically, it is more difficult to explain low carbon and oxygen abundances relative to the planet's host star via disk migration than via disk-free migration (Madhusudhan et al. 2014). The high eccentricity of TOI-172 b is suggestive of disk-free migration, although our investigation of its orbital evolution suggests it never possessed the extremely high eccentricity that would be required to migrate from a formation location beyond the ice line. Moreover, as discussed previously, it is plausible that many hot Jupiters migrated first in the disk and then consequently through planet–planet interactions; even eccentric planets may have disk migration in their history. Nonetheless, there are currently only about a dozen planets larger than Neptune for which the eccentricity is greater than 0.2 with at least 99% confidence, a relatively short period (<20 days), and are bright enough ($V < 12$) to be well suited for atmospheric characterization (see footnote 42). Interestingly, less than half of these systems (including TOI-172) have a massive planetary companion ($>3\,M_J$). Therefore, TOI-172 b—with the other few known planets in this subsample, such as HAT-P-2b (Bakos et al. 2007) and WASP-162 (Hellier et al. 2019)—provides a great opportunity to carry out this test. If a depletion of oxygen and carbon are detected, it could provide evidence that it migrated via a disk-free method, or otherwise place constraints on its disk migration history. Future observations could try to characterize the composition of TOI-172 b's atmosphere using current facilities like the *Hubble Space Telescope* and future facilities like the *James Webb Space Telescope*. Additionally, understanding the full architecture of the TOI-172 system, by looking for long-period giant planet companions through RV monitoring, may provide additional insight into its evolutionary history.

5. Conclusion

We present the discovery of TOI-172 b, a massive Jupiter in a highly eccentric $\sim$9.5-day orbit around a slightly evolved G star. The planet has a very high density ($M_P = 5.42^{+0.22}_{-0.20}\,M_J$, $R_P = 0.965^{+0.032}_{-0.029}\,R_J$, $\rho_P = 7.53^{+0.65}_{-0.72}$ g cm^{-3}) while its host star appears to be a subgiant ($M_\star = 1.128^{+0.065}_{-0.061}\,M_\odot$, $R_\star = 1.777^{+0.047}_{-0.044}\,R_\odot$, $\log g = 3.993^{+0.027}_{-0.028}$). Interestingly, TOI-172 b is in a rare class of highly eccentric (>0.3), short-period (<20 days) massive ($>3\,M_J$) planets. The large mass and semimajor axis of TOI-172 b corresponds to a circularization timescale much larger than the age of the universe. The large eccentricity of the planet's orbit suggests that at least some of its migration history included dynamical interactions with other components in the system. From studying the orbital evolutionary history of TOI-172 we are unable to place any useful constraints on Q_P or $Q^\star$ since the tidal evolution is expected to be slow in this system for all reasonable values of $Q^\star$ and Q_P. Future observations could provide more evidence for the migration mechanism by studying the atmospheric composition of TOI-172 b or by studying the entire known ensemble of hot Jupiters in the literature.

Facilities: TESS, FLWO 1.5 m (Tillinghast Reflector Echelle Spectrograph), 4.1-m Southern Astrophysical Research (SOAR), LCO 0.4 m, LCO 1.0 m, 2.2 m telescope La Silla (Fiber-fed Extended Range Optical Spectrograph).

Software: EXOFASTv2 (Eastman et al. 2013; Eastman 2017), AstroImageJ (Collins et al. 2017).

ORCID iDs

Joseph E. Rodriguez ⓘ https://orcid.org/0000-0001-8812-0565
Samuel N. Quinn ⓘ https://orcid.org/0000-0002-8964-8377
Chelsea X. Huang ⓘ https://orcid.org/0000-0003-0918-7484
Andrew Vanderburg ⓘ https://orcid.org/0000-0001-7246-5438
Kaloyan Penev ⓘ https://orcid.org/0000-0003-4464-1371
Rafael Brahm ⓘ https://orcid.org/0000-0002-9158-7315
Andrés Jordán ⓘ https://orcid.org/0000-0002-5389-3944
David W. Latham ⓘ https://orcid.org/0000-0001-9911-7388
Keivan G. Stassun ⓘ https://orcid.org/0000-0002-3481-9052
Avi Shporer ⓘ https://orcid.org/0000-0002-1836-3120
Carl Ziegler ⓘ https://orcid.org/0000-0002-0619-7639
Jason D. Eastman ⓘ https://orcid.org/0000-0003-3773-5142
B. Scott Gaudi ⓘ https://orcid.org/0000-0003-0395-9869
Karen A. Collins ⓘ https://orcid.org/0000-0001-6588-9574
Thomas Barclay ⓘ https://orcid.org/0000-0001-7139-2724
Allyson Bieryla ⓘ https://orcid.org/0000-0001-6637-5401
L. G. Bouma ⓘ https://orcid.org/0000-0002-0514-5538
Patricia T. Boyd ⓘ https://orcid.org/0000-0003-0442-4284
Jennifer Burt ⓘ https://orcid.org/0000-0002-0040-6815
Michael L. Calkins ⓘ https://orcid.org/0000-0002-2830-5661
Jessie Christiansen ⓘ https://orcid.org/0000-0002-8035-4778
Knicole D. Colón ⓘ https://orcid.org/0000-0001-8020-7121
Tansu Daylan ⓘ https://orcid.org/0000-0002-6939-9211
Diana Dragomir ⓘ https://orcid.org/0000-0003-2313-467X
Néstor Espinoza ⓘ https://orcid.org/0000-0001-9513-1449
Ana Glidden ⓘ https://orcid.org/0000-0002-5322-2315
Maximilian N. Günther ⓘ https://orcid.org/0000-0002-3164-9086
Jon M. Jenkins ⓘ https://orcid.org/0000-0002-4715-9460
Nicholas M. Law ⓘ https://orcid.org/0000-0001-9380-6457
Andrew W. Mann ⓘ https://orcid.org/0000-0003-3654-1602
Edward H. Morgan ⓘ https://orcid.org/0000-0003-1447-6344
Ryan J. Oelkers ⓘ https://orcid.org/0000-0002-0582-1751
Martin Paegert ⓘ https://orcid.org/0000-0001-8120-7457
Joshua Pepper ⓘ https://orcid.org/0000-0002-3827-8417
Paula Sarkis ⓘ https://orcid.org/0000-0001-8128-3126
Joshua E. Schlieder ⓘ https://orcid.org/0000-0001-5347-7062
Lizhou Sha ⓘ https://orcid.org/0000-0001-5401-8079
Andrei Tokovinin ⓘ https://orcid.org/0000-0002-2084-0782
Guillermo Torres ⓘ https://orcid.org/0000-0002-5286-0251
Roland K. Vanderspek ⓘ https://orcid.org/0000-0001-6763-6562
Steven Villanueva, Jr. ⓘ https://orcid.org/0000-0001-6213-8804
Joshua N. Winn ⓘ https://orcid.org/0000-0002-4265-047X
Ian Wong ⓘ https://orcid.org/0000-0001-9665-8429
Liang Yu ⓘ https://orcid.org/0000-0003-1667-5427
Zhuchang Zhan ⓘ https://orcid.org/0000-0002-4142-1800
George Zhou ⓘ https://orcid.org/0000-0002-4891-3517

References

Adams, F. C., & Laughlin, G. 2006, ApJ, 649, 1004
Akeson, R. L., Chen, X., Ciardi, D., et al. 2013, PASP, 125, 989
Batygin, K. 2012, Natur, 491, 418
Batygin, K., Bodenheimer, P. H., & Laughlin, G. P. 2016, ApJ, 829, 114
Becker, J. C., Vanderburg, A., Adams, F. C., Rappaport, S. A., & Schwengeler, H. M. 2015, ApJL, 812, L18
Bensby, T., Feltzing, S., & Lundström, I. 2003, A&A, 410, 527
Boley, A. C. 2009, ApJL, 695, L53
Bonomo, A. S., Desidera, S., Benatti, S., et al. 2017, A&A, 602, A107
Borucki, W. J., Koch, D., Basri, G., et al. 2010, Sci, 327, 977
Boss, A. P. 2000, ApJL, 536, L101
Brahm, R., Jordán, A., & Espinoza, N. 2017, PASP, 129, 034002
Brown, T. M., Baliber, N., Bianco, F. B., et al. 2013, PASP, 125, 1031
Buchhave, L. A., Bakos, G. Á, Hartman, J. D., et al. 2010, ApJ, 720, 1118
Buchhave, L. A., Latham, D. W., Carter, J. A., et al. 2011, ApJS, 197, 3
Buchhave, L. A., Latham, D. W., Johansen, A., et al. 2012, Natur, 486, 375
Choi, J., Dotter, A., Conroy, C., et al. 2016, ApJ, 823, 102
Ciardi, D. R., Beichman, C. A., Horch, E. P., & Howell, S. B. 2015, ApJ, 805, 16
Coşkunoğlu, B., Ak, S., Bilir, S., et al. 2011, MNRAS, 412, 1237
Collins, K. A., Kielkopf, J. F., Stassun, K. G., & Hessman, F. V. 2017, AJ, 153, 77
Crida, A., & Batygin, K. 2014, A&A, 567, A42
Cutri, R. M., Skrutskie, M. F., van Dyk, S., et al. 2003, yCat, 2246, 0
D'Angelo, G., Kley, W., & Henning, T. 2003, ApJ, 586, 540
Dawson, R. I., & Johnson, J. A. 2018, ARA&A, 56, 175
Dawson, R. I., & Murray-Clay, R. A. 2013, ApJL, 767, L24
Dawson, R. I., Murray-Clay, R. A., & Johnson, J. A. 2015, ApJ, 798, 66
Dotter, A. 2016, ApJS, 222, 8
Eastman, J. 2017, EXOFASTv2: Generalized Publication-quality Exoplanet Modeling Code, Astrophysics Source Code Library, ascl:1710.003
Eastman, J., Gaudi, B. S., & Agol, E. 2013, PASP, 125, 83
Fabrycky, D., & Tremaine, S. 2007, ApJ, 669, 1298
Fűrész, G. 2008, PhD thesis, University Szeged, Hungary
Gaia Collaboration, Brown, A. G. A., Vallenari, A., et al. 2016, A&A, 595, A2
Gaia Collaboration, Brown, A. G. A., Vallenari, A., et al. 2018, A&A, 616, A1
Gammie, C. F. 2001, ApJ, 553, 174
Haisch, K. E., Jr., Lada, E. A., & Lada, C. J. 2001, ApJL, 553, L153
Hellier, C., Anderson, D. R., Bouchy, F., et al. 2019, MNRAS, 482, 1379
Høg, E., Fabricius, C., Makarov, V. V., et al. 2000, A&A, 355, L27
Howell, S. B., Sobeck, C., Haas, M., et al. 2014, PASP, 126, 398
Huang, C., Wu, Y., & Triaud, A. H. M. J. 2016, ApJ, 825, 98
Huang, C. X., Hartman, J. D., Bakos, G. Á, et al. 2015, AJ, 150, 85
Jenkins, J. M., Twicken, J. D., McCauliff, S., et al. 2016, Proc. SPIE, 9913, 99133E
Jensen, E. 2013, Tapir: A Web Interface for Transit/Eclipse Observability, Astrophysics Source Code Library, ascl:1306.007
Kaufer, A., Stahl, O., Tubbesing, S., et al. 1999, Msngr, 95, 8
Knutson, H. A., Fulton, B. J., Montet, B. T., et al. 2014, ApJ, 785, 126
Bakos, G. Á, Kovács, G., Torres, G., et al. 2007, ApJ, 670, 826
Kovács, G., Zucker, S., & Mazeh, T. 2002, A&A, 391, 369
Kurucz, R. L. 1992, in IAU Symp. 149, The Stellar Populations of Galaxies, ed. B. Barbuy & A. Renzini (Dordrecht: Kluwer), 225
Lissauer, J. J., & Stevenson, D. J. 2007, in Protostars and Planets V, ed. B. Reipurth, D. Jewitt, & K. Keil (Tucson, AZ: Univ. Arizona Press), 591
Lutz, T. E., & Kelker, D. H. 1973, PASP, 85, 573
Madhusudhan, N., Amin, M. A., & Kennedy, G. M. 2014, ApJL, 794, L12
Monet, D. G., Levine, S. E., Canzian, B., et al. 2003, AJ, 125, 984
Nagasawa, M., & Ida, S. 2011, ApJ, 742, 72
Nidever, D. L., Marcy, G. W., Butler, R. P., Fischer, D. A., & Vogt, S. S. 2002, ApJS, 141, 503
Papaloizou, J. C. B., Nelson, R. P., Kley, W., Masset, F. S., & Artymowicz, P. 2007, in Protostars and Planets V, ed. B. Reipurth, D. Jewitt, & K. Keil (Tucson: Univ. Arizona Press), 655

Paxton, B., Bildsten, L., Dotter, A., et al. 2011, ApJS, 192, 3
Paxton, B., Cantiello, M., Arras, P., et al. 2013, ApJS, 208, 4
Paxton, B., Marchant, P., Schwab, J., et al. 2015, ApJS, 220, 15
Penev, K., Zhang, M., & Jackson, B. 2014, PASP, 126, 553
Pollack, J. B., Hubickyj, O., Bodenheimer, P., et al. 1996, Icar, 124, 62
Quinn, S. N., White, R. J., Latham, D. W., et al. 2014, ApJ, 787, 27
Rasio, F. A., & Ford, E. B. 1996, Sci, 274, 954
Ricker, G., & Vanderspek, R. 2018, Data Products From TESS Data Alerts,
     https://archive.stsci.edu/prepds/tess-data-alerts/index.html
Ricker, G. R., Winn, J. N., Vanderspek, R., et al. 2015, JATIS, 1, 014003
Schlaufman, K. C., & Winn, J. N. 2016, ApJ, 825, 62
Schlegel, D. J., Finkbeiner, D. P., & Davis, M. 1998, ApJ, 500, 525
Skrutskie, M. F., Cutri, R. M., Stiening, R., et al. 2006, AJ, 131, 1163
Stassun, K. G., Oelkers, R. J., Pepper, J., et al. 2018, AJ, 156, 102

Stassun, K. G., & Torres, G. 2018, ApJ, 862, 61
Steffen, J. H., Ragozzine, D., Fabrycky, D. C., et al. 2012, PNAS, 109,
     7982
Tokovinin, A. 2018, PASP, 130, 035002
Torres, G., Bakos, G. Á, Kovács, G., et al. 2007, ApJL, 666, L121
Vanderburg, A., & Johnson, J. A. 2014, PASP, 126, 948
Vanderburg, A., Latham, D. W., Buchhave, L. A., et al. 2016, ApJS, 222, 14
Winn, J. N., Fabrycky, D., Albrecht, S., & Johnson, J. A. 2010, ApJL,
     718, L145
Wu, Y., & Lithwick, Y. 2011, ApJ, 735, 109
Wu, Y., & Murray, N. 2003, ApJ, 589, 605
Yu, L., Zhou, G., Rodriguez, J. E., et al. 2018, AJ, 156, 250
Zacharias, N., Finch, C., & Frouard, J. 2017, AJ, 153, 166
Ziegler, C., Law, N. M., Baranec, C., et al. 2018, AJ, 155, 161